POPULAR SUMMARY

Retrieval of aerosol optical depth above clouds from OMI observations: sensitivity analysis, case studies
Submitted to Journal of the Atmospheric Sciences

O. Torres[1], H. Jethva[2] and P.K. Bhartia[1]
[1]NASA Goddard Space Flight Center, Code 614
[2] GESTAR/USRA

Aerosols are tiny particles, such as smoke, soil dust, and sea salt, suspended in the atmosphere. They scatter and absorb solar radiation and play an important role in the energy balance of the earth-atmosphere system. Carbonaceous particles produced by biomass burning and boreal forest fires, and desert dust particulate originated in the arid and semi-arid regions are the most predominant light absorbing aerosol types. The UV Aerosol index detects the presence of absorbing aerosols. A large fraction of the atmospheric aerosol load reaches the free troposphere and is frequently located above clouds.

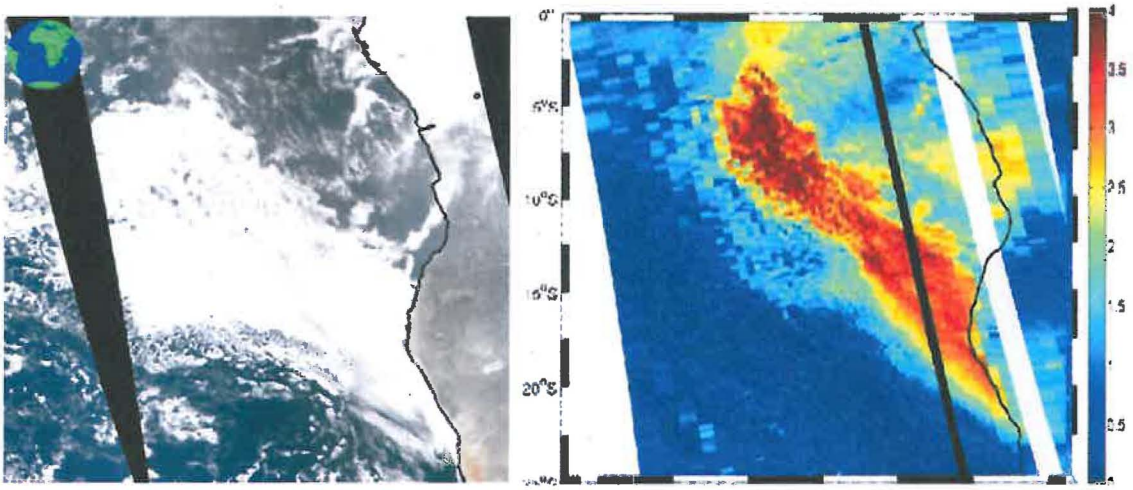

Figure 1: An absorbing aerosol layer as seen from space by two satellite sensors on August 4, 2007 over the South Atlantic Ocean off the coasts of Angola and Namibia : Aqua-MODIS visible image of an extended low level cloud (left); Aura-OMI detection of a smoke layer above clouds in terms of the UV aerosol index.

A variety of well established space and ground based techniques are used to measure the amount (i.e., optical depth) of suspended particle matter under cloud-free conditions. Aerosol above clouds, however, can only be measured from airborne or satellite-based instrumentation.

We have developed a method to measure the optical depth of light-absorbing smoke and dust aerosols located above clouds using satellite observations of upwelling radiation at two wavelengths in the near-UV spectral range (330-390 nm) used to calculate the UV Aerosol Index. The technique takes advantage of the particle's large absorption capacity of cloud reflected radiation to detect and quantify particulate matter above clouds.

Carbonaceous and dust aerosols above clouds absorb a fraction of the radiation reflected by the cloud and can, thus, produce a net warming effect of the atmospheric column. The magnitude of the resulting warming depends on the aerosol optical depth and its absorption capacity. The measuring technique developed here provides a very important remote sensing tool to accurately quantify the atmospheric aerosol load above clouds. The improved AOD estimates will allow a better characterization

the direct radiative forcing of above-cloud-aerosols, and a better understanding of other aspects of aerosol-cloud interaction.

Retrieval of Aerosol Optical Depth above Clouds from OMI Observations: Sensitivity Analysis and Case Studies

Omar Torres[1], Hiren Jethva[2] and P.K. Bhartia[1]

[1]NASA Goddard Space Flight Center, Greenbelt, MD, 20771
[2]Department of Atmsospheric and Planetary Sciences, Hampton University

Abstract

A large fraction of the atmospheric aerosol load reaching the free troposphere is frequently located above low clouds. Most commonly observed aerosols above clouds are carbonaceous particles generally associated with biomass burning and boreal forest fires, and mineral aerosols originated in arid and semi-arid regions and transported across large distances, often above clouds. Because these aerosols absorb solar radiation, their role in the radiative transfer balance of the earth atmosphere system is especially important. The generally negative (cooling) top of the atmosphere direct effect of absorbing aerosols, may turn into warming when the light-absorbing particles are located above clouds. The actual effect depends on the aerosol load and the single scattering albedo, and on the geometric cloud fraction. In spite of its potential significance, the role of aerosols above clouds is not adequately accounted for in the assessment of aerosol radiative forcing effects due to the lack of measurements. In this paper we discuss the basis of a simple technique that uses near-UV observations to simultaneously derive the optical depth of both the aerosol layer and the underlying cloud for overcast conditions. The two-parameter retrieval method described here makes use of the UV aerosol index and reflectance measurements at 388 nm. A detailed sensitivity analysis indicates that the measured radiances depend mainly on the aerosol absorption exponent and aerosol-cloud separation. The technique was applied to above-cloud aerosol events over the Southern Atlantic Ocean yielding realistic results as indicated by indirect evaluation methods. An error analysis indicates that for typical overcast cloudy conditions and aerosol loads, the aerosol optical depth can be retrieved with an accuracy of approximately 54% whereas the cloud optical depth can be derived within 17% of the true value.

1. Introduction

Because of the nature of the physical processes driving the emission and atmospheric injection of desert dust and carbonaceous aerosols, i.e., the wind's lifting power of soil particles over arid and semi-arid areas and the strong convective activity associated with anthropogenic biomass burning and wild fire events, large amounts of these light-absorbing particles reach the free troposphere more often than other aerosol types that generally reside in the boundary layer such as sulfate and sea salt aerosols. Elevated layers of desert dust and carbonaceous particulate are therefore frequently observed above clouds where they are mobilized by the prevailing winds and transported thousands of kilometers away from their original sources. The spring and summer transoceanic transport of desert dust across the Atlantic Ocean and the spring flow of aerosol from Asian sources across the Pacific Ocean to North America and sometimes reaching Northern Europe have been well documented using both satellite observations [*Kaufman et al. , 2005*], as well as model calculations [*Kallos et al., 2006; Johnson et al., 2010*]. Smoke layers originating from well-known regional sources of agricultural biomass burning mainly in Africa and South America *[Duncan et al.,* 2003; *Torres et al.,* 2010]. Smoke layers can also be the result of wild fires in both hemispheres [*Colarco et al.,* 2004; *Dirksen et al.*, 2009] that are transported across the oceans or from northern to mid-latitudes from their original distant remote sources to populated centers where they often contribute to the observed high levels of local pollution [*Jaffe et al.*, 2004]. Elevated aerosol layers, often lofted above clouds, are also observed in connection with pyro-convective events [*Fromm et al.,* 2008]. Much of the long range transport of desert

73 dust and carbonaceous aerosols, however, takes place above low level layers of
74 altostratus and stratocumulus clouds.

75 Quantifying the fraction of the atmospheric aerosol load above clouds is important for
76 air quality considerations as some of these aerosols eventually descend into the boundary
77 layer contributing to the enhancement of pollution levels. Knowledge of the amount and
78 type of aerosol above clouds is also of interest for radiative forcing considerations. The
79 general cooling effect of these aerosol types under clear sky conditions may turn into a
80 warming effect when located above clouds. Depending on their light absorption capacity
81 above-cloud-aerosols may have a positive radiative forcing effect at the top of the
82 atmosphere [*Keil and Haywood, 2003; Haywood and Shine, 1997*; *Chand et al., 2008*],
83 whose magnitude depends on the aerosol single scattering albedo and cloud fraction in
84 addition to the total aerosol load. *Liao and Seinfeld* [1998a, 1998b] examined the
85 radiative forcing of desert dust and found out that the highest radiative forcing occurs
86 for dust layers located above clouds. This effect is particularly important for
87 carbonaceous aerosols in which the combined absorption effect of its organic (OC) and
88 black (BC) carbon components acts on the incoming solar radiation from the UV to the
89 near-IR producing potentially large effects on the local climate. The radiative effect of
90 carbonaceous aerosols above stratiform clouds off the coasts of Angola and Namibia was
91 estimated during the SAFARI 2000 field experiment making use of radiative transfer
92 calculations [*Keil and Haywood,* 2003] and airborne-measured profiles of aerosol particle
93 number concentration, scattering coefficients, and meteorological parameters [*Haywood*
94 *et al.*, 2003]. The study indicated that the normally cooling effect of the smoke aerosol
95 layer of about -13 Wm^{-2} over a cloud free area turned into a warming effect of 11.5 Wm^{-2}

96 for the same aerosol layer located above a cloud deck which is similar to the expected
97 radiative forcing effect associated with an increase in surface albedo. Changes in cloud
98 morphology may also result as a consequence of atmospheric heating (by aerosol
99 absorption) of the air above the cloud deck. As suggested by *Wilcox* [2010], this
100 aerosol-induced heating of the atmosphere may lead to the optical thickening of the cloud
101 resulting from enhanced liquid water path and lower cloud top associated with the
102 warming above the cloud.

103 Agriculture-related biomass burning in the tropical regions accounts for nearly 80 %
104 of the global amount including both anthropogenic and naturally produced burning [*Hao*
105 *and Liu*, 1994]. It is estimated that although BC above clouds makes up 20% of the total
106 burden, it accounts for about 50% of the BC radiative forcing effect [*Zarcichy and Bond,*
107 2010]. To properly estimate the regional and global forcing effect of carbonaceous and
108 desert dust aerosols it is therefore necessary to quantify the atmospheric aerosol load
109 above clouds.

110 In this paper we present a method of deriving aerosol optical depth over clouds
111 making use of near-UV observations by the Ozone Monitoring Instrument (OMI) on the
112 Aura satellite. The high near-UV sensitivity to aerosol absorption [*Torres et al., 1998;*
113 *2007*] is further enhanced in the presence of underlying clouds due to the high reflectance
114 from the cloud-top layer. A general description of the near-UV capability of aerosol
115 detection is presented in section 2 followed by a detailed discussion of a sensitivity
116 analysis of near-UV observations to aerosol presence above clouds in section 3. A
117 description of the retrieval procedure and error analysis is presented in section 4, and

118 results of application of the inversion procedure to two case studies are discussed in
119 section 5. Discussion and conclusion are presented in section 6.
120
121 **2. Satellite detection of aerosols above clouds.**
122 The detection and characterization of aerosols in cloud-free scenes using near-UV
123 satellite observations is an established aerosol remote sensing technique developed based
124 on Total Ozone Mapping Spectrometer (TOMS) observations [*Torres et al.,* 1998]. The
125 near-UV technique is particularly sensitive to absorbing aerosols as explained below. A
126 long-term record (1979-1992/1996-2001) of aerosol optical depth [*Torres et al.,* 2002]
127 was developed from TOMS observations. Currently, OMI near-UV observations are
128 used in the OMAERUV algorithm to derive aerosol optical depth (AOD) and single
129 scattering albedo (SSA) under cloud-free conditions [*Ahn et al.,* 2008; *Torres et al.,*
130 2007]. In this paper we describe initial results of a recently developed approach using
131 OMI observations to derive the optical depth of aerosol layers above clouds.
132 Aerosols above clouds, or for that matter above any bright background, are not
133 easily detectable by conventional satellite remote sensing approaches that measure
134 aerosols based on the increased reflectance associated with particle scattering. The
135 difficulty lies on the fact that aerosol scattering contribution to the total upwelling
136 reflectance at the top of the atmosphere is very small compared to the reflectance of the
137 bright cloud background. Thus, to be able to separate the aerosol scattering signal from
138 the measured total, one should be able to characterize the reflective properties of the
139 bright background (i.e., clouds) to a level of accuracy probably unachievable. Aerosol

140 absorption effects, however, can be advantageously used for the detection and
141 characterization of absorbing particles even over highly reflective backgrounds.
142 It has been demonstrated that aerosols that absorb UV radiation can be detected
143 and characterized using the unambiguous particle absorption signal in the measured
144 levels of UV reflectance [*Torres et al.,* 1998]. The unique advantage of the near-UV
145 detection capability of absorbing aerosols is the large Rayleigh scattering component that
146 makes available for absorption by aerosol particles a significantly larger number of
147 photons than at longer wavelengths [*Torres et al.,* 1998]. The most commonly known
148 near-UV aerosol product is the absorbing aerosol index (AAI), a parameter used to detect
149 UV-absorbing aerosols over ocean and all land surfaces.
150 The AAI was developed as a byproduct of improvements to the column ozone
151 amount retrieval algorithm applied to UV observations by the TOMS instrument. It is
152 basically a residual quantity resulting from the comparison between measured and
153 calculated radiances in the range 330-390 nm where trace gas absorption effects are
154 negligible. The calculated radiance is obtained using a simple model of the earth-
155 atmosphere system consisting of a molecular atmosphere bounded at the bottom by a
156 Lambert Equivalent Reflector (LER) [*Dave and Mateer*, 1967]. The LER reflectivity ρ is
157 derived from measurements at wavelength λ_0. A key assumption in this model
158 representation of the earth-atmosphere system is that the reflectivity of the column
159 atmosphere's lower boundary is wavelength independent in the near UV. This
160 hypothetical surface is intended to account for the wavelength dependent effects of
161 surface, clouds, and aerosols which are not explicitly included in the radiative transfer
162 calculations.

163 The residue, r_λ is defined as the natural log of the ratio of the actually measured

164 radiance L_λ^* to the calculated value L_λ^{cal} assuming an effective surface reflectivity ρ_{λ_0},

165 $$r_\lambda = -100 \log\left[\frac{L_\lambda^*}{L_\lambda^{cal}(\rho_{\lambda_0})}\right] \quad (1).$$

166 This residual quantity provides a measure of the error in predicting the actually observed
167 spectral contrast using the LER model. Examination of global maps of the residue
168 clearly indicate that UV-absorbing aerosols are by far the most important residue source
169 [*Hsu et al.,* 1996; *Herman et al.,* 1997] and has become a powerful tool of absorbing
170 aerosols detection that has been used in a variety of applications. Hence, the term
171 Absorbing Aerosol Index was coined to refer to this residual quantity. The AAI is the
172 same as r_λ when $\lambda_0 > \lambda$, and it is defined as $-r_\lambda$ when $\lambda_0 < \lambda$ so that it is always
173 positive in the presence of absorbing aerosols. In the OMAERUV algorithm AAI is
174 calculated for $\lambda_0 = 388$ nm and $\lambda = 354$ nm.

175 The AAI detection capability of absorbing aerosols is not limited to cloud-free,
176 dark scenes. It can also identify the presence of absorbing particles above bright
177 backgrounds such as ice-snow covered surfaces and cloud decks. Figure 1 shows a
178 typical aerosol-above-cloud event on August 4, 2007 over the Southern Atlantic Ocean as
179 seen by three different A-train sensors. The top panel depicts the OMI UV Aerosol Index
180 indicating the unmistakable presence of an absorbing aerosol layer above the horizontally
181 extended cloud feature shown in the Aqua-MODIS (Moderate Resolution Imaging
182 Spectro-radiometer) true color image composite (bottom panel). The cloud layer covers a
183 large region from the coast of Namibia and Angola extending into the ocean in a north-
184 west direction. The center panel illustrates the vertical distribution of clouds and aerosols

185 in terms of the CALIOP (Cloud Aerosol LIdar with Ortogonal Polarization) lidar 532 nm
186 attenuated backscatter measured along the CALIPSO (Cloud-Aerosol Lidar and Infrared
187 Pathfinder Satellite Observation) spacecraft orbital track shown on both the OMI and
188 MODIS images. The CALIOP's transect shows the presence of a geometrically thin low
189 level cloud with cloud-top at 1 km above sea level. An aerosol layer at about 2 km above
190 the cloud is observed over the first half of the image. Towards the middle of the shown
191 orbital section the aerosol layer is observed over a cloud free area.

192 TOMS and OMI AAI observations over clouds have been used in conjunction
193 with other satellite measurements to estimate the radiative effects of aerosol layers above
194 clouds [*Hsu et al.*, 2003; *Peters et al.,* 2009]. Other applications include the use of
195 SCIAMACHY derived AAI for identification of aerosol layers above cloud and the
196 analysis of aerosol absorption effect on visible and near-IR TOA radiance
197 measurements by the same sensor [*de Graaf et al.*, 2007].

198 Aerosols above clouds have also been detected and their optical depth estimated by
199 polarization measurements by the POLDER sensor [*Waquet et al.,* 2009]. This approach
200 uses multi-sensors measurements aboard A-train constellation to derive aerosol optical
201 depth above cloud taking advantage of the unique angular dependence associated with the
202 presence of the polarized radiation of above-cloud-aerosols. The modification in the
203 polarized light reflected by cloud top by the aerosol layer allows retrieving aerosol
204 optical depth using a single scattering approximation for aerosol signal.

205 Active space-borne measurements can also be used to derive the optical depth of
206 aerosols above clouds. The standard CALIOP AOD product is derived as the vertically
207 integrated aerosol extinction coefficient over the vertical extent of the identified aerosol

208 feature. This approach requires an assumption of the extinction-to-backscatter or lidar
209 ratio [*Kittaka et al,* 2011]. Alternate transmission methods for directly deriving AOD
210 above clouds from CALIOP observations of depolarization [*Hu et al,* 2007] and color
211 [*Chand et al,* 2008] ratios have been investigated. Unlike the standard approach, the
212 transmission-based lidar techniques do not require assumption on the lidar ratio.
213
214 **3.0 Sensitivity Analysis**
215 *3.1 Aerosol and Cloud Models*
216 In this section we discuss the results of a sensitivity analysis of the near-UV
217 reflectance at the top of the atmosphere to aerosol and cloud properties. Radiative transfer
218 calculations at 354 and 388 nm were carried out for an atmosphere containing both
219 aerosols and clouds using the Vector Linearized Discrete Ordinate Radiative Transfer
220 code (VLIDORT) developed by *Spurr* [2006]. VLIDORT calculates Jacobians and
221 radiances for reflectances at the top of a multilayered atmosphere. It takes into account
222 the atmosphere's curvature making use of a pseudo-spherical approximation for solar
223 beam attenuation and includes a sphericity correction for off-nadir viewing at large
224 angles. The VLIDORT code accounts for multiple scattering effects by molecules,
225 aerosols and clouds.
226 In the following discussion, the cloud droplet size distribution is represented by
227 the C1 modified Gamma distribution suggested by *Deirmendjian* (1964) which is
228 commonly used in clouds radiative transfer modeling [*Rossow and Schiffer,* 1999;
229 *Ahmad et al.,* 2004]. The assumed distribution with a maximum radius of 15 μm yields a
230 6.0 μm radiatively effective radius. Two aerosol models representative of carbonaceous

231 aerosols are used in the calculations. The assumed bi-modal particle size distributions and
232 complex refractive index of the selected aerosol models are based on multiyear
233 AERONET (Aerosol Robotic Network) statistics of measurements at locations where
234 carbonaceous aerosols are typically observed [*Dubovik, et al.,* 2002]. AERONET
235 retrievals of aerosol particle size and optical properties use both direct sun and sky
236 radiance measurements as input to an inversion algorithm [*Dubovik and King*, 2000]. The
237 reported measurements are representative of the atmospheric column aerosol load and
238 are therefore suitable for the analysis of space-borne remotely sensed data. The first
239 model, representative of black carbon (BC), has a wavelength independent imaginary
240 refractive index, while the second one assumes a wavelength dependent absorption
241 refractive index associated with organic carbon (OC) consistent with observations
242 [*Kirchstetter et al.,* 2004]. Table 1 lists the aerosol parameters used in the calculations.
243 A 0.5 km thick cloud located between 1 and 1.5 km above sea level (900 and 850
244 hPa respectively) is assumed. The aerosol vertical distribution is represented by a single
245 layer whose concentration follows a Gaussian distribution characterized by the height of
246 maximum concentration (peak) and full-width-half-maximum. Note that this yields an
247 aerosol profile in which the entire aerosol load is located above the cloud. The above
248 described vertical distribution of clouds and aerosols resembles actual conditions
249 observed by the CALIOP lidar over the Southern Atlantic Ocean as shown in Figure 1.
250
251 *3.2 Reflectance sensitivity to aerosol type and cloud parameters*
252 The sensitivity of the satellite measured reflectance at 354 and 388 nm to cloud-
253 top height was first examined in the no-aerosol case. For a cloud of optical depth 10,

254 systematically varying cloud top level between 950 and 100 mb produced maximum
255 differences of -3% reflectance at 354 nm and -1% at 388 nm resulting from the
256 shielding by clouds of molecular scattering. Negligible reflectance change was observed
257 associated with variations in cloud drop effective radius.

258 Figure 2 shows the calculated top of the atmosphere reflectance at 388 nm as a
259 function of cloud optical depth (COD) for a column atmosphere containing cloud layer
260 between 1.0 and 1.5 km and an aerosol layer with peak particle concentration at 3 km
261 above the surface and a full-width at half maximum of 0.5 km. Results for a no-aerosol
262 case and two different absorbing aerosol models of optical depth 1 (at 388 nm) are
263 presented.

264 The solid line in Figure 2 depicts the relationship between the calculated TOA
265 388 nm reflectance, and cloud optical depth for COD between 0 and 50. The observed
266 reflectance increases monotonically with COD as expected. The cloud diffuse radiation is
267 by far the most important source of the observed TOA reflectance enhancement.
268 Although molecular and aerosol scattering are also present [*Wen et al.,* 2008], their
269 contribution to the observed TOA reflectance for overcast conditions, which may be
270 important for optically thin clouds, is negligible at large values of cloud optical depth.

271 The results associated with an aerosol layer of single scattering albedo of 0.95
272 (at 388 nm) representative of BC are indicated by the dotted line in Figure 2. For weakly
273 absorbing aerosols, scattering dominates over absorption effects and the net result is an
274 increase of TOA reflectance values above those of the cloud-only case for optically thin
275 clouds. Aerosol scattering and absorption effects cancel each other at a COD value of
276 about 5. At larger COD values the increased cloud reflectance triggers additional aerosol

277 absorption, resulting in TOA reflectance values lower than the ones for the no-aerosol
278 case. For the largest modeled COD (50) the weakly absorbing aerosol produces a 16%
279 TOA decrease in relation to the no-aerosol case. For a stronger absorbing aerosol case
280 (SSA=0.85) the absorption effect dominates over scattering even at low COD values as
281 indicated by the dashed line in Figure 2. For a COD value of 50, the observed TOA
282 reflectance is reduced by 33%.

283 *3.3 Aerosol Index sensitivity to spectral aerosol absorption.*

284 The resulting AAI for clouds only and above-clouds absorbing aerosol layers are
285 shown in Figure 3. For clouds only the AAI is slightly negative, reaching a value of -0.6
286 at COD 5. It then increases with increasing COD, becoming zero at COD 20 and reaching
287 about 0.25 at COD 50. Although the AAI of clouds depends on observing geometry
288 (solar and viewing zenith angles, and relative azimuth angle), for solar zenith angles
289 lower than 60, it oscillates around zero between -1.0 and 1.0 (not shown) with the
290 slightly negative values associated with COD smaller than about 20 and small positive
291 values for larger COD's. These results shown in Figure 3 are consistent with previously
292 reported sensitivity analysis using Mie Theory [*Torres et al.,* 1998; *Herman et al.,* 1997]
293 that show the weak spectral dependence associated with the scattering effects of non-
294 absorbing large size particles. For typical AOD values, large aerosol particles yield
295 AAI's close to zero whereas for non-absorbing aerosol particles smaller than about 0.3
296 μm and typical AOD values the resulting AAI is negative reaching values as low as about
297 -1 for large aerosol loads. The slightly larger cloud-only AAI values in Figure 3 than
298 reported by *Torres et al* [1998] are due to the much larger optical depth of clouds.

299 The small AAI values calculated for cloud droplets in the current work differ
300 from recently published calculations [*Penning de Vries et al,* 2009] in which clouds are
301 reported to produce negative AAI values (as large as -1.5) for all values of COD. A
302 likely explanation for the noted discrepancy is the *Penning de Vries et al.* approximate
303 representation of the angular dependence of scattering by clouds and aerosols using a
304 Henyey-Greenstain (H-G) phase function instead of actual Mie calculations. Using the
305 H-G function to represent clouds does not allow to account for the angular effects
306 associated with varying size of the scattering particle [*Hansen,* 1969].
307 For absorbing aerosols located above clouds, the radiative coupling between
308 cloud diffuse radiation, molecular scattering, and particle absorption enhances the
309 observed near UV spectral contrast and, therefore, the resulting AAI is larger than the one
310 associated with the same aerosol layer under cloud-free conditions. The AAI magnitude
311 will also depend on the spectral dependence of aerosol absorption as determined by the
312 wavelength dependence of the imaginary component of the index of refraction. The
313 effect of the above-cloud absorbing aerosols on the calculated AAI as a function of COD
314 for several values of the Angstrom Absorption Exponent (AAE) [*Bond,* 2001] and SSA
315 0.85 (388 nm) is also shown in Figure 3. In all cases the calculated positive AAI is a
316 strong function of the COD of the underlying cloud layer. The slope of the observed
317 COD-AAI relationship decreases for COD values larger than 20. The resulting AAI
318 values increase rapidly as the AAE varies from a value of 1.0 (dotted line), an indicator
319 of non-wavelength dependent imaginary refractive index (representative of BC), to
320 values of 2.0 (dot-dash line), and 2.8 (dashed line) representative of wavelength-

dependent aerosol absorption. A detailed analysis of the AAI sensitivity to spectral aerosol absorption is presented in *Jethva and Torres* [2011].

The presence of organic carbon (OC) in the carbonaceous aerosols produced by biomass burning has been demonstrated by a variety of laboratory and field studies [*Kirchstetter et al.*, 2004; *Hoffer et al*, 2006; *Russell et al.*, 2010]. A recent analysis combining OMI near UV observations, radiative transfer calculations and ground-based measurements of aerosol optical depth [*Jethva and Torres*, 2011] has further confirmed the presence of OC as an important aerosol component of biomass-burning generated smoke. *Jethva and Torres* [2011] showed that allowing for the wavelength dependence of the imaginary refractive index in the near-UV (an indication of OC presence) produced significantly better agreement of OMI retrieved AOD with sun-photometer observations than when using an aerosol model with wavelength independent imaginary refractive index characteristic of black carbon. Thus, the OC aerosol model has been selected as more representative of the actual carbonaceous aerosol load in the OMAERUV algorithm. In the remainder of this work we will use the OC aerosol model.

3.4 Aerosol Index Sensitivity to Aerosol-cloud separation

The AAI dependence on aerosol layer height over cloudless scenes is a well documented AAI property [*Torres et al, 1998*; *Degraaf et al,* 2005]. We will now examine the resulting height dependence when the absorbing aerosol layer lies above a cloud deck of varying reflectance as determined by the COD. As in the preceding analysis, the cloud layer is located between 1.0 and 1.5 km. The height of the absorbing aerosol layer is assumed to be 2.5, 3.0, 4.0 and 5.0 km above the surface. The resulting relative change in AAI value as a function of aerosol layer height and COD is depicted in

Figure 4. Largest percent change is observed for the cloud-free case (COD = 0) and quickly goes down with increasing COD. For a COD value of 30, the AAI associated with a height change of 2.5 km is about 25 %, compared to more than 75% for the cloud-free case. Thus, unlike in the cloud-free case where the aerosol layer height is a large source of uncertainty for the quantitative interpretation of the AAI [*Torres et al,* 1998], in the presence of underlying clouds the AAI sensitivity to aerosol layer height is reduced. The inset in figure 4b illustrates the rate of change of AAI per 1km change in aerosol layer height as a function of cloud optical depth. The observed rapid drop in AAI sensitivity to cloud-aerosol separation with increasing COD is an advantage from retrieval point of view as it introduces less uncertainty in the derivation of AOT due to wrong assumption on the aerosol height above the cloud.

4. Retrieval Approach

4.1 Simultaneous aerosol-cloud retrieval

It the preceding sections it has been shown that the magnitude of the observed AAI associated with aerosol layers above clouds depends on the reflectance of the underlying cloud (COD), the aerosol load (AOD) and single scattering albedo, the AAE parameter, and the aerosol-cloud separation. For testing of the current research retrieval algorithm the values of some of these parameters can be prescribed based on independent observations. Aerosol-cloud separation, for instance, is obtainable from space-borne CALIOP lidar profiles. A justifiable assumption of the 388 nm single scattering albedo can be made from retrievals by the cloud-free OMAERUV algorithm [*Torres et al.,* 2007] in the vicinity of the cloud-aerosol feature under investigation assuming this value

367 to be representative of the SSA of the above-cloud aerosol load. Assumption on the value
368 of the AAE parameter is required. In principle, COD information from other sensors in
369 the A-train (i.e., MODIS) could be used as input to the inversion algorithm. This option,
370 however, implies the use of erroneous COD data as the MODIS cloud optical product
371 will be most probably also affected by the absorption effects of the overlying aerosol
372 layer [*Wilcox et al.*, 2009]. In this work we demonstrate a retrieval approach that
373 accounts for the spatial variability of clouds and aerosols by simultaneously deriving
374 AOD and COD over overcast scenes covered by opaque clouds.
375 The retrieval scheme uses a set of pre-calculated values of AAI and 388 nm
376 reflectances for several values of COD (0, 2, 5, 10, 20, 30, 40, 50), and AOD (0, 0.1, 0.5,
377 1.0, 2.5, 4.0) for a fixed value of SSA and assumed AAE. Cloud and aerosol layer heights
378 are prescribed based on CALIPSO observations. With the above stated assumptions the
379 interpolating domain reduces to a two dimensional array on COD and AOD as illustrated
380 in Figure 5. As shown on the web-like diagram, an observation set of AAI and the 388
381 nm reflectance is associated with a set of values of COD and AOD.
382
383 *4.2 Error Analysis*
384 The accuracy of the retrieved parameters depends on the uncertainty associated
385 with the assumed values of aerosol layer height above the cloud and the wavelength-
386 dependent aerosol single scattering albedo. In this section we discuss the results of an
387 error analysis assuming a set of 'true' conditions consisting of an aerosol layer of known
388 optical depth and single scattering albedo located at a height Z above the surface, and a
389 0.5 km thick cloud layer with cloud top at 1.5 km and known optical depth. The assumed

390 cloud-aerosol vertical structure is representative of the typically observed cloud-aerosol
391 layers over the Southern Atlantic-Ocean off the coasts of Angola and Namibia during
392 that region's biomass burning season [*King et al.*, 2003; *Chand et al,* 2009]. The
393 uncertainty on the spectrally dependent single scattering albedo is evaluated by assuming
394 a fixed SSA value at 388nm and an associated AAE value that describes the wavelength
395 dependence of the aerosol absorption optical depth. The true value of Z is assumed to be
396 4km. A SSA value of 0.85 typical of biomass burning smoke aerosols for this region [*Eck*
397 *et al.*, 2003] , and an AAE value of 2.2 as reported by *Kirchstetter et al.*, [2004] during
398 SAFARI 2000 field campaign are assumed. Radiative transfer calculations were carried
399 out for a nominal AOD value of 0.5, and COD values of 5 and 10. The assumed values
400 of Z and SSA are perturbed by ±2km and ±0.03 respectively that represent typical
401 variability associated with these parameters [*Chand, et al* 2009; *Eck et al,* 2003] over the
402 Southern Atlantic region . The assumed AAE parameter is varied between 1.8 and 2.6 or
403 ±0.4 to account for possible variations in aerosol composition (i.e., OC content).
404 Although the actual natural variability of AAE is largely unknown the tested range allows
405 accounting for some uncertainty on its actual value. The AAE perturbation is equivalent
406 to a change from the nominal spectral dependence of 15% in the values of the imaginary
407 refractive index (i.e., $k_{354} = 1.15 k_{388}$) to 10% and 20%.

408 The obtained AOD and COD retrieval errors associated with the assumed range
409 of uncertainty of the prescribed parameters are shown in Table 2. For a nominal COD
410 value of 5, maximum AOD retrieval errors take place when Z is underestimated (40%),
411 SSA is overestimated (48%), and AAE is underestimated (23%) yielding a combined
412 largest AOD error estimate of 67%. Minimum AOD errors, on the other hand, result

413 when Z and AAE are overprescribed and SSA is underestimated producing a combined
414 AOD under-estimation error of about -34%. The overall AOD error goes down with
415 increasing cloud optical depth. For a more typical COD value of 10 the overall AOD
416 error range decreases to -27 to 54%.
417 Expected errors in retrieved COD are smaller than those associated with the AOD
418 retrieval. For a nominal COD value of 5 the overall error range associated with the above
419 described uncertainties -4 to 7%, and gets larger as the cloud becomes optically ticker.
420 An error range between -6 to 17% is expected for COD 10.
421
422 **5. Case studies**
423 *5.1 Cloud-only case: October 13, 2006*
424 We will first examine the near-UV capability of retrieving COD from single
425 channel-measurements. This test is necessary to assess the results of the combined AOD-
426 COD retrieval algorithm discussed in this section. In the absence of intervening aerosols
427 cloud optical depth can be derived from solar reflectance measurements at wavelengths
428 where gas absorption interference is negligible. Cloud optical depth is routinely derived
429 from MODIS observations on the Terra and Aqua satellites at 860 nm over the oceans
430 and 645 nm over land [*Platnick et al.,* 2003]. In the cloud-only retrieval application the
431 observations are inverted using the forward calculations for AOD zero shown in Figure 5.
432 This is equivalent to a single channel retrieval using OMI's 388 nm reflectance
433 measurements. This approach was used to derive the optical depth of the cloud field over
434 the Southern Atlantic Ocean on October 13, 2006. To ensure that broken clouds were
435 excluded, the retrieval was only applied to those OMI scenes characterized by overcast

436 conditions or unity MODIS geometric cloud fraction (CF). The absence of absorbing
437 aerosols above the clouds was verified by making sure the AAI was close to zero. A
438 comparative analysis of MODIS geometric CF and OMI 388 nm reflectivity (introduced
439 in section 2) indicated that overcast conditions can be present at OMI reflectivity (ρ)
440 values as low as 0.20. Thus, a 0.20 minimum ρ threshold value was used. OMI retrieved
441 COD was compared with collocated MODIS COD observations. Given the large
442 difference in spatial resolution between the two sensors (MODIS 0.5X0.5 km^2 versus
443 OMI 13x24 km^2) linear averaging of the MODIS COD product over the OMI pixel was
444 necessary. Data points in Figure 6 are color-coded as a function of the associated OMI
445 derived reflectivity. The comparison of the OMI research COD (388 nm) and MODIS
446 operational COD (860 nm) products in Figure 6 indicates a close agreement between the
447 retrievals with correlation coefficient 0.92 and slope 0.96. The OMI COD values appear
448 slightly lower than those from MODIS for R values lower than 0.30 probably associated
449 with the presence of broken and/or transparent clouds. The close OMI-MODIS agreement
450 in retrieved COD illustrates the sensitivity of OMI observations to cloud presence and is
451 consistent with the reported agreement in effective CF calculated by *Stammes et al*
452 [2008] from MODIS retrieved geometric CF [*Platnick et al.*, 2003] and OMI retrieved
453 effective CF from observations of O_2-O_2 absorption at 477 nm [*Acarreta et al*, 2004].
454
455 *5.2 Aerosols above clouds: August 4, 2007*
456 The presence of smoke layers above stratocumulus clouds off the coasts of
457 Namibia and Angola is a common occurrence during the biomass burning season from
458 August thru October. Low level stratus clouds form a few hundred meters above sea

459 level. Since the continental surface is about 1 km above sea level, westward smoke
460 advection results in the accumulation of carbonaceous aerosols above low level clouds.
461 The retrieval method described in section 4 has been applied to the aerosol event depicted
462 in Figure 1. Note that during this event a section of the aerosol strip detected by CALIOP
463 is located above a thin, spatially continuous cloud deck at 1 km above sea level (between
464 about 21°S and 11°S) whereas cloudy and cloud-free conditions are intermittently present
465 below the aerosol layer between 11°S and 5°S. Cloud presence above the aerosol layer is
466 observed north of 5°S. For retrieval purposes, CALIOP observations shown in Figure 1
467 have been used to prescribe cloud location (top 1.5 km, bottom 1 km) and aerosol layer
468 height (3km). A 388 nm aerosol SSA value of 0.88 has been assumed based on
469 OMAERUV algorithm retrieval [*Torres et al.,* 2007] over a cloud free region at 12°S,
470 10°E. The spectral dependence of near-UV aerosol absorption has been characterized
471 based on the work by *Kirchstetter et al* [2004] who found that an AAE value of about -
472 2.2 adequately described the spectral dependence of aerosol absorption optical depth of
473 carbonaceous particles resulting from biomass burning during the SAFARI-2000
474 campaign [*Swap et al,* 2003]. An AAE value of -2.2 is equivalent to a 14% increase in
475 imaginary refractive index from 388 to 354 nm as assumed in this analysis. Retrievals
476 were carried out for OMI scenes with R larger than 0.20 and AAI values larger than
477 unity. Note that in the presence of absorbing aerosols above clouds, the actual cloud
478 reflectivity is likely larger than the OMI observed one.
479 Figure 7 depicts the retrieved AOD (Figure 7a) and COD (Figure 7b) fields. The
480 number of possible retrievals is limited by the upper limit COD limit of 50 currently used
481 in the research retrieval algorithm. Therefore for COD's larger than 50, neither COD nor

482 AOD values are reported. A clear south-north gradient in the obtained AOD is observed
483 across the aerosol layer with minimum values in the 0.3-0.6 range along the southern
484 edge of the layer and maxima of 1.8 or larger along the northern boundary of the aerosol
485 layer. The COD field shows three localized areas of COD larger than about 12 whereas
486 the COD background values of about 5 to 10 predominate everywhere else.

487 A qualitative assessment of the derived aerosol optical depth can be done by
488 examining certain characteristics of the retrieved AOD and COD fields to obtain an idea
489 of the reliability of the results or the lack thereof. A quick visual inspection of the spatial
490 variability of the two retrieved quantities indicates that the derived AOD and COD fields
491 are not generally correlated. For instance, low AOD and high COD values are observed at
492 the region in the vicinity of 14°S, 2°E, whereas the opposite scenario (i.e., high AOD and
493 low COD values) occurs in the area surrounding the clear area at 12°S, 7°E.

494 Since Aqua-MODIS and Aura-OMI observations are only a few minutes apart,
495 one can evaluate the OMI COD retrieval by directly comparing it to MODIS results. As it
496 was previously demonstrated in this work, when no aerosols are found above clouds OMI
497 retrieved COD is in excellent agreement with the MODIS operational COD product
498 (Figure 6). In spite of the difference in spatial resolution between the two sensors the
499 different cloud features in the MODIS product are easily recognizable in the OMI COD
500 image (not shown). A scatter plot of retrieved COD by the two sensors is shown in Figure
501 8. Because of the aerosol absorption effect on the MODIS 860 nm reflectance [*Wilcox et*
502 *al.*,2009], OMI retrieved COD values are expected to be higher than those of MOD IS.
503 Overall a good level of agreement between the two retrievals is observed as indicated by
504 the high t correlation coefficient (0.85), near-one slope (1.07) and low y-intercept (-

505 0.19). A careful analysis in terms of cloud reflectivity shows that for ρ values less than
506 0.25 (blue filled circles) OMI consistently retrieves lower-than-MODIS COD 's. This
507 result probably indicates that OMI clouds of reflectivity less 0.25 are either non-opaque
508 or non-uniform (i.e., broken clouds), or both, which would allow radiation from below
509 the cloud or from cloud-free parts of the pixel reach the sensor producing an
510 underestimate of the cloud optical depth. For clouds with reflectivity between 0.25 and
511 0.30 (green triangles) OMI and MODIS COD tend to be in agreement for COD values up
512 to about 7. At larger values the OMI COD is again underestimated in relation to MODIS
513 probably due to no meeting the required overcast conditions. Thus, it seems that for ρ
514 values less than 0.30, the overcast and opaque cloud condition is not met and, therefore,
515 the OMI COD error is comparable to or larger than the aerosol absorption induced error
516 in the MODIS product. For ρ values larger than 0.30 (red crosses), on the other hand,
517 OMI consistently retrieves higher than MODIS values for COD values up to 15. The
518 lower MODIS values are most probably associated with the aerosol absorption effects at
519 860 nm that would result in the underestimation of the optical depth as discussed by
520 *Wilcox et al* [2009]. Figure 9 shows a scatter plot between AOD and AAI, indicating the
521 expected high correlation between these two quantities.

522 Another way of qualitatively assessing the retrieved AOD fields is to analyze the
523 spatial continuity between cloudy and cloud-free areas. An inherent assumption made
524 here is that the AOD field does not change significantly from overcast scene to the
525 adjacent clear region. Here, we employ standard OMAERUV algorithm to derive AOD
526 fields over cloud-free region. Figure 10 shows a composite of AOD retrievals over
527 cloudy and cloud-free scene. No obvious spatial discontinuities in AOD along the

528 northern edge of cloudy region and adjacent clear region are observed. Missing data,
529 however, is observed along the northernmost edge of the cloud and, especially over the
530 southernmost boundary in the transition from overcast to totally clear conditions. The
531 occurrence of these pockets of missing data is expected as none of the OMI algorithms
532 deal with partial cloudiness conditions.
533
534 *5.3 Aerosols above clouds: August 31, 2005*
535 A second sample retrieval was carried out for an aerosol event on August 31,
536 2005 over the same region. Similar assumptions on aerosol-cloud vertical distribution to
537 those in the August 4-2007 case were used for this event. A 388nm SSA value of 0.90
538 retrieved over a clear area at 16°S, 14°E was assumed together with an AAE exponent of
539 -2.2 as in the previously discussed example.
540 The MODIS true color image composite and the OMI AAI data on August 31
541 2005 (not shown) illustrate the presence of a smoke layer located above a large
542 horizontally extended cloud deck over the Southern Atlantic Ocean. Retrieved AOD and
543 COD fields for this event are depicted in Figure 11. The shown AOD field includes
544 retrievals under both overcast and cloud free conditions. Peak AOD values larger than
545 3.0 are observed over the southeastern region of the cloud off the coast of Namibia
546 where cloud optical depth values in the vicinity of 5 were retrieved. Lower AOD values
547 of about 1.0 are observed over the optically densest part of the cloud where the COD
548 reaches values close to 20. As in the previous case no correlation between the retrieved
549 AOD and COD fields is observed. The OMI retrieved COD again correlates very well
550 with the MODIS COD product as shown in Figure 12. As in the previous case, the OMI-

551 derived COD is generally higher than the MODIS retrieval for reflectivity larger than
552 0.30 and, somewhat lower than the MODIS results for lower reflectivity values. In this
553 case, larger OMI-MODIS differences are observed than on the August 4, 2007 case
554 which is consistent with the retrieved larger aerosol load.

555 *5.4 Assessment of AOD results*

556 The validation of satellite retrievals of aerosol optical depth is only possible by
557 means of sun-photometer measurements as it is routinely done to validate space-borne
558 quantification of the atmospheric aerosol load. For a direct quantitative assessment of
559 above-cloud aerosol optical depth retrievals, as reported in this work, airborne sun-
560 photometer measurements [*Russell et al,* 2005] would be required. In the absence of
561 those observations, however, a semi-quantitative evaluation can be attempted by
562 comparing the OMI obtained AOD results to those obtained by other satellite-based
563 techniques capable of detecting, and possibly quantifying, aerosol amounts above clouds.
564 Such retrievals have been attempted by application of active [*Kittaka et al.*, 2011; *Chand*
565 *et al.,* 2008] CALIOP observations as well as passive POLDER measurement of
566 polarized radiation [*Waquet et al.,* 2008] described in section 2.

567 A comparison of the CALIOP version 3.01 standard AOD (532 nm) to OMI AOD
568 at 388 nm for the August 4 2007 case discussed in section 5.2 was carried out. Although
569 a correlation between the two retrievals is apparent, the standard CALIOP AOD is
570 significantly smaller than the OMI results. The wavelength difference does not explain
571 the large observed differences. Given the current provisional nature of the CALIOP
572 AOD product as indicated by the official CALIPSO Quality Statement, we defer further
573 evaluation of OMI above-cloud-aerosol retrievals using CALIOP data as a future work

574 activity when a more definitive CALIOP AOD product may be available. Results of
575 above-cloud-aerosol optical depth by the method described here were compared to an
576 equivalent POLDER AOD product as described by [*Waquet et al,* 2008]. Figure 13
577 shows a scatter plot of POLDER AOD at 865 nm to OMI's 388 nm for the event of
578 August 4 2008 documented in *Waquet et a*l [2008]. A well defined correlation between
579 the two measurements is observed. Although OMI retrieved AOD's are about three times
580 as large as POLDER's, the difference can be explained by the small aerosol particle size
581 typical of carbonaceous aerosols and the difference in reporting wavelength. A reduction
582 of results to a common wavelength (not shown) indicates a close one-to-one agreement.
583

584 **6.0 Summary and conclusions**

585 We have discussed the basis, and presented examples, of an inversion procedure
586 to derive the optical depth of the atmospheric aerosol load above clouds. The retrieval
587 technique uses measurements of backscattered near-UV measurements by the OMI
588 sensor on the Aura satellite. The OMI-derived absorbing aerosol index and the observed
589 388 nm reflectance are fed to an inversion procedure that simultaneously retrieves both
590 aerosol and cloud optical depth. Results of a sensitivity analysis indicate that the
591 magnitude of the aerosol index associated with absorbing aerosols above clouds depends
592 on cloud and aerosol optical depth, wavelength dependent aerosol single scattering
593 albedo (or AAE) and, to a lesser extent on aerosol layer-cloud separation. Thus, to
594 simultaneously retrieve AOD and COD, assumptions on the values of the other
595 parameters or external information on them is needed. An error analysis was carried out
596 to estimate the uncertainty in the retrieved values of aerosol and cloud optical depth

597 associated with the uncertainty in the assumed values of single scattering albedo and
598 aerosol cloud separation. Results indicate that the combined uncertainty of ±0.03 in
599 single scattering albedo and ±2km in aerosol-cloud separation yields an AOD error
600 between -26% and 54% for typical cloud and aerosol layer optical depth of 10 and 0.5
601 respectively. Retrieval errors decrease with increasing cloud optical depth. Errors in
602 retrieved COD are smaller than 20% in most cases which are comparable to the reported
603 uncertainty of the MODIS product for optical depths larger than about 10 [*Platnick et al,*
604 2003].

605 The retrieval approach was applied to two aerosol events over the Southern
606 Atlantic Ocean off the West coast of Southern Africa on August 4, 2007 and August 31
607 2005 where a persistent widespread layer of carbonaceous aerosols transported from the
608 adjacent land region accumulates above a uniform low-level stratocumulus could deck
609 during August and September. In the absence of airborne sun photometer measurements
610 for a direct assessment of the validity of the retrieved AOD results, a qualitative analysis
611 was carried out. For both events the OMI retrieved AOD and COD fields are uncorrelated
612 with each other which indicate the absence of retrieval biases associated with the bright
613 reflecting background. An examination of the spatial homogeneity of the AOD retrieval
614 over overcast and cloud-free scenes August 4 2007 shows no obvious discontinuities in
615 the clear-to-cloudy transition regions except for the expected lack of retrievals over partly
616 cloudy scenes.

617 Direct comparisons of MODIS and OMI retrieved cloud optical depths during
618 both events show a very good correlation. When the satellite derived scene reflectivity is
619 lower than about 0.25 OMI retrieved COD's are smaller than those of MODIS indicating

620 the presence in the OMI scene of broken and/or transparent clouds. For scene
621 reflectivities larger than 0.30, overcast opaque cloud conditions seem to exist and OMI
622 COD retrievals are higher than those of MODIS. The larger OMI COD values are
623 consistent with the expected error in MODIS COD associated with the effect of aerosol
624 absorption on the near-IR radiances (860 nm) used in the retrieval. The good correlation
625 between the two COD measurements and the explainable difference in OMI-MODIS
626 retrieval results lends confidence to the results of the OMI two- parameter retrieval given
627 that the OMI and MODIS COD retrieval approaches are fundamentally different from
628 each other.

629 A quantitative evaluation of the derived AOD was carried out by comparing OMI
630 AOD results to equivalent CALIOP and POLDER retrievals. The comparison to the
631 lidar-based product was not conclusive due to the current provisional nature of the
632 CALIOP AOD product. The comparison to POLDER results, on the other hand, yielded a
633 very high correlation. The observed difference in magnitude of the two measurements
634 can be explained in terms of the predominantly small aerosol particles and the difference
635 in reporting wavelengths.
636

636 **References**

637 Acarreta, J.R., J. F. De Haan, and P. Stammes (2004), Cloud pressure retrieval using the
638 O_2-O_2 absorption band at 477 nm, *J. Geophys. Res.*, 109, D05204,
639 doi:10.1029/2003JD003915.

640 Ahmad, Z., P. K. Bhartia, and N. Krotkov (2004), Spectral properties of backscattered
641 UV radiation in cloudy atmospheres, *J. Geophys. Res.*, 109, D01201,
642 doi:10.1029/2003JD003395.

643 Ahn C., O. Torres, and P.K. Bhartia (2008), Comparison of OMI UV Aerosol Products
644 with Aqua-MODIS and MISR observations in 2006, *J. Geophys. Res*, 113, D16S27,
645 doi:10.1029/2007JD008832.

646 Bond, T.C., (2001), Spectral dependence of visible light absorption by carbonaceous
647 particles emitted from coal combustion, *Geophys. Res. Lett.* 28(21): 4075–4078.

648 Chand, D., T. L. Anderson, R. Wood, R. J. Charlson, Y. Hu, Z. Liu, and M. Vaughan
649 (2008), Quantifying above-cloud aerosol using spaceborne lidar for improved
650 understanding of cloudy-sky direct climate forcing, *J. Geophys. Res.*, 113, D13206,
651 doi:10.1029/2007JD009433.

652 Chand D., R. Wood, T.L. Anderson, S.K. Satheesh, and R.J. Charlson (2009) Satellite-
653 derived direct radiative effect of aerosols dependent on cloud cover, Nature
654 Geoscience Letters, doi:10.10.138

655 Colarco, P., M. Schoeberl, B. Doddridge, L. Marufu, O. Torres, and E. Welton. Transport
656 of Smoke from Canadian Forest Fires to the Surface near Washington, D.C.: Injection

657 Height, Entrainment, and Optical Properties, *J. Geophys. Res.,* 109, D06203,
658 doi:10.1029/2003JD004248, 2004.
659 Dave, J.V., and C.L. Mateer (1967), A preliminary study on the possibility of
660 estimating total atmospheric ozone from satellite measurements, *J. Atm Sci.,* 24,
661 414-427
662 de Graaf, M., P. Stammes, O. Torres, and R. B. A. Koelemeijer (2005), Absorbing
663 Aerosol Index: Sensitivity analysis, application to GOME and comparison with TOMS, J.
664 Geophys. Res., 110, D01201, doi:10.1029/2004JD005178.
665 de Graaf, M., P. Stammes, and E. A. A. Aben (2007), Analysis of reflectance spectra of
666 UV-absorbing aerosol scenes measured by SCIAMACHY, *J. Geophys. Res.*, 112,
667 D02206, doi:10.1029/2006JD007249.

668 Deirmendjian, D. (1964),Scattering and polarization properties of water clouds and
669 hazes in the visible and infrared, *Appl. Opt.,* 3, 187–196, 1964.

670 Dirksen, R.J, K. Folkert Boersma, J. de Laat, P. Stammes, G.R. van der Werf, M. Val
671 Martin, and H.M. Kelder (2009), An aerosol boomerang: Rapid around-the-world
672 transport of smoke from the December 2006 Australian forest fires observed from space,
673 *J. Geophys. Res.,* 114, D21202, doi:10.1029/2009JD012360
674 Dubovik, O., and M.D. King (2000), A flexible inversion algorithm for retrieval of
675 aerosol optical properties from sun and sky radiance measurements. , *J. Geophys. Res,*
676 105, 20673-20696.
677 Dubovik, O., et al. (2002), Variability of absorption and optical properties of key aerosol
678 types observed in worldwide locations, *J. Atmos. Sci.,* 59, 590– 608.

679 Duncan, B. N., R. V. Martin, A. C. Staudt, R. Yevich, and J. A. Logan (2003),
680 Interannual and seasonal variability of biomass burning emissions constrained by satellite
681 observations, *J. Geophys. Res.*, 108(D2), 4100, doi:10.1029/2002JD002378.
682 Eck, T.F et al. (2003), Variability of biomass burning aerosol optical characteristics in
683 southern Africa during the SAFARI 2000 dry season campaign and a comparison of
684 single scattering albedo estimates from radiometric measurements, *J. Geophys. Res.*, 108,
685 8477, doi:10.1029/2002JD002321.
686 Fromm, M., O. Torres, D. Diner, D. Lindsey, B. Vant Hull, R. Servranckx, E. P. Shettle,
687 and Z. Li (2008), Stratospheric impact of the Chisholm pyrocumulonimbus eruption: 1.
688 Earth-viewing satellite perspective, *J. Geophys. Res,* 113, D08202,
689 doi:10.1029/2007JD009153.
690 Hansen, J.E. (1969), Exact and approximate solutions for multiple scattering by cloudy
691 and hazy planetary atmospheres, *J. Atmos. Sci.*, 26, 478- 487
692 Haywood, J. M., and K. P. Shine (1997), Multi-spectral calculations of the direct
693 radiative forcing of tropospheric sulphate and soot aerosols using a column model, *Q. J.*
694 *R. Meteorol. Soc.*, 123, 1907 –1930.
695 Haywood J. M., S. Osborne, P. N. Francis, A. Kiel, P. Formenti, T. W. Andreae, and P.
696 Kaye (2003), Mean physical and optical properties of regional haze dominated by
697 biomass burning aerosol measured from the C-130 aircraft during SAFARI 2000, *J.*
698 *Geophys. Res.,* 108, doi:10.1029/ 2002JD002226.
699 Hao, W. M., and M.-H. Liu (1994), Spatial and temporal distribution of tropical
700 biomass burning, *Global Biol. Cycles*, 8, 495 –503.

701 Herman JR, PK Bhartia, O Torres, C Hsu, C Seftor, and E Celarier (1997) Global
702 distribution of UV-absorbing aerosols from Nimbus 7/TOMS data. *J. Geophys. Res.* 102:
703 16911–16922.
704 Hoffer, A., Gelencs´er, A., Guyon, P., Kiss, G., Schmid, O., Frank, G. P., Artaxo, P., and
705 Andreae, M. O. (2006), Optical properties of humic-like substances (HULIS) in biomass-
706 burning aerosols, Atmos. Chem. Phys., 6, 3563–3570.
707 Hsu NC, JR Herman, PK Bhartia, CJ Seftor, O Torres, AM Thompson, JF Gleason, TF
708 Eck, and BN Holben (1996) Detection of Biomass Burning Smoke from TOMS
709 Measurements.
710 Hsu, N.C., J.R.Herman, and Si-Chee Tsay (2003), Radiative impacts from biomass
711 burning in the presence of clouds during boreal Spring in southeast Asia, *Geophys. Res.*
712 *Lett.*, 30, doi:10.1029/2002GL016485
713 Hu, Y, M. Vaughan, Z. Liu, K. Powell, and S. Rodie r (2007) ,Retrieving Optical Depths
714 and Lidar Ratios for Transparent Layers Above Opaque Water Clouds From CALIPSO
715 Lidar Measurements, *IEEE Geosci. Remote Sens. Lett.*, **4**, 523-526.
716 Jaffe, D., I. Bertschi, L. Jaegle´, P. Novelli, J. S. Reid, H. Tanimoto, R. Vingarzan, and
717 D. L. Westphal (2004), Long-range transport of Siberian biomass burning emissions and
718 impact on surface ozone in western North America, *Geophys. Res. Lett.,* 31, L16106,
719 doi:10.1029/2004GL020093.
720 Jethva, H. and Torres, O (2011): Satellite-based evidence of wavelength-dependent
721 aerosol absorption in biomass burning smoke inferred from ozone monitoring instrument,
722 Atmos. Chem. Phys. Discuss., 11, 7291-7319, doi:10.5194/acpd-11-7291-2011.

723 Johnson, M. S., N. Meskhidze, F. Solmon, S. Gassó, P. Y. Chuang, D. M. Gaiero, R. M.
724 Yantosca, S. Wu, Y. Wang, and C. Carouge (2010), Modeling dust and soluble iron
725 deposition to the South Atlantic Ocean, J. Geophys. Res., 115, D15202,
726 doi:10.1029/2009JD013311.
727 Kallos, G., A. Papadopoulos, P. Katsafados, and S. Nickovic (2006), Transatlantic
728 Saharan dust transport: Model simulation and results, J. Geophys. Res., 111, D09204,
729 doi:10.1029/2005JD006207.
730 Kaufman, Y. J., I. Koren, L. A. Remer, D. Tanre´, P. Ginoux, and S. Fan (2005), Dust
731 transport and deposition observed from the Terra-Moderate Resolution Imaging
732 Spectroradiometer (MODIS) spacecraft over the Atlantic Ocean, J. Geophys. Res., 110,
733 D10S12, doi:10.1029/2003JD004436.
734 Keil, A., and J. M. Haywood (2003), Solar radiative forcing by biomass burning aerosol
735 particles during SAFARI 2000: A case study based on measured aerosol and cloud
736 properties J. Geophys. Res., 108(D13), 8467, doi:10.1029/2002JD002315, 2003.
737 King, M.D., S. Platnick, C. C. Moeller, H. E. Revercomb, and D. A. Chu (2003),
738 Remote sensing of smoke, land, and clouds from the NASA ER-2 during SAFARI 2000,
739 *J. Geophys. Res.*, 108, 8502, doi:10.1029/2002JD003207.
740 Kirchstetter, T. W., T. Novakov, and P. V. Hobbs (2004), Evidence that the spectral
741 dependence of light absorption by aerosols is affected by organic carbon, J. Geophys.
742 Res., 109, D21208, doi:10.1029/2004JD004999.
743 Kittaka. C., D.M. Winker, M.A. Vaughan, A. Omar, and L. A. Remer (2011),
744 Intercomparison of column aerosol optical depths from CALIPSO and MODIS-Aqua,
745 Atmos. Meas. Tech., 4, 131-141.

746 Liao, H., and J. H. Seinfeld (1998a), Effect of clouds on direct aerosol radiative forcing
747 of climate, *J. Geophys. Res.,* 103, 3781 –3788.
748 Liao, H., and J. H. Seinfeld (1998b), Radiative forcing by mineral dust aerosol:
749 Sensitivity to key variables, *J. Geophys. Res.,* 103, 31,637 – 31,646.
750 Penning de Vries, M.J.M, S. Beirle, and T. Wagner, (2009), UV Aerosol Indices from
751 SCIAMACHY: introducing the SCattering Index (SCI), Atmos. Chem. Phys., 9, 9555–9567
752 Peters, K., Quaas, J., and Bellouin, N. (2009), Effects of absorbing aerosols in cloudy
753 skies: a satellite study over the Atlantic Ocean, Atmos. Chem. Phys., 11, 1393-1404,
754 doi:10.5194/acp-11-1393-2011.
755 Platnick, S., M. D. King, A. Ackerman, W. P. Menzel, B. A. Baum, J. C. Riédi, and R. A.
756 Frey (2003), The MODIS cloud products: Algorithms and examples from Terra, *IEEE*
757 *Trans. Geosci. Remote Sens.*, 41, 459– 473.
758 Rossow, W.B., and R.A. Schiffer (1999), Advances in understanding clouds from ISCCP,
759 *Bull. Am. Meteorol. Soc.,* 80, 2261-2287.
760 Russell, P.B. et al., (2005), Aerosol Optical Depth measurements by airborne sun
761 photometer in SOLVE II: Comparison to SAGE III, POAM III and airborne spectromter
762 measurements, Atmos. Chem. Phys., 5, 1311-1339.
763 Russell, P. B., Bergstrom, R. W., Shinozuka, Y., Clarke, A. D., DeCarlo, P. F.,
764 Jimenez, J. L., Livingston, J. M., Redemann, J., Dubovik, O., and Strawa, A (2010),
765 Absorption Angstrom Exponent in AERONET and related data as an indicator of aerosol
766 composition, Atmos. Chem. Phys., 10, 1155-1169, doi:10.5194/acp-10-1155-2010
767 Spurr RJD, VLIDORT: a linearized pseudo-spherical vector discrete ordinate radiative
768 transfer code for forward model amd retrieval studies in multilayer multiple scattering
769 media, *JQSRT* 102(2), 316-342, 2006.

770 Stammes P., M. Sneep, J.F. de Haan, J.P. Veefkind, P. Wang, and P. Levelt (2008)
771 Effective cloud fractions from the Ozone Monitoring Instrument: Theoretical framework
772 and validation, *J. Geophys. Res.,* 113, D16S38, doi:10.1029/2007JD008820.
773 Swap, R. J., H. J. Annegarn, J. T. Suttles, M. D. King, S. Platnick, J. L. Privette, and R. J.
774 Scholes (2003), Africa burning: A thematic analysis of the Southern African Regional
775 Science Initiative (SAFARI 2000), J. Geophys. Res., 108(D13), 8465,
776 doi:10.1029/2003JD003747.
777 Torres O, PK Bhartia, JR Herman, Z Ahmad, and J Gleason (1998) Derivation of aerosol
778 properties from satellite measurements of backscattered ultraviolet radiation: Theoretical
779 basis. *J. Geophys. Res*. 103: 17099.
780 Torres O, PK Bhartia, JR Herman, A Sinyuk, and B Holben (2002) A long term record of
781 aerosol optical thickness from TOMS observations and comparison to AERONET
782 measurements. *J. Atm. Sci.* 59:398–413.
783 Torres, O., A. Tanskanen, B. Veihelman, C. Ahn, R. Braak, P. K. Bhartia, P. Veefkind,
784 and P. Levelt (2007), Aerosols and Surface UV Products from OMI Observations: An
785 Overview, , *J. Geophys. Res.,* 112, D24S47, doi:10.1029/2007JD008809.
786 Torres, O., Z. Chen, H. Jethva, C. Ahn, R. Freitas, and P.K. Bhartia (2010), OMI and
787 MODIS observations of the anomalous 2008-2009 Southern Hemisphere biomass
788 burning seasons, *Atmos. Chem. Phys.* 10, 3505-3513
789 Waquet, F., J. Riedi, L.C. Labonnote, P. Goloub, B. Cairns, J.L. Deuze, and D. Tanre
790 (2009) Aerosol Remote Sensing over Clouds using A-train Observations, *J. Atm.*
791 *Sci.*,doi:10.1175/2009JAS3026.1

792 Wen, G., A. Marshak, and R. F. Cahalan (2008), Importance of molecular Rayleigh
793 scattering in the enhancement of clear sky reflectance in the vicinity of boundary layer
794 cumulus clouds, *J. Geophys. Res.*, 113, D24207, doi:10.1029/2008JD010592.
795
796 Wilcox, E. M., Harshvardhan, and S. Platnick (2009), Estimate of the impact of
797 absorbing aerosol over cloud on the MODIS retrievals of cloud optical thickness and
798 effective radius using two independent retrievals of liquid water path, *J. Geophys.*
799 *Res.*, 114, D05210, doi:10.1029/2008JD010589.
800 Wilcox, E. M. (2010), Stratocumulus cloud thickening beneath layers of absorbing smoke
801 aerosol. Atmos. Chem. Phys., 10, 11769-11777,doi:10.5194/acp-10-11769-2010.
802 Zarczcky, C.M. and T.M. Bond (2010) How much can the vertical distribution of black
803 carbon affect its global direct radiative forcing? *Geophys. Res. Lett.*, 37, L20807,
804 doi:10.1029/2010GL044555
805
806 Acknowledgements
807 The authors thank F. Waquet from the Universitè des Sciences et Technologies de Lille
808 for making available retrieval results from POLDER measurements for comparison to our
809 results. We are also thankful to the valuable feedback of three anonymous reviewers.
810

Table 1.

Model	r_f (μm)	σ_f (μm)	N_f (cm^{-2})	r_c(μm)	σ_c (μm)	N_c (cm^{-2})	Refractive Index
BC aerosol	0.08	1.49	10.3	0.7	2.08	0.0021	1.50+0.015
OC aerosol	0.08	1.49	10.3	0.7	2.08	0.0021	1.50+0.015 (388 nm) 1.50+0.018 (354nm)

Aerosol parameters: mode radius(r), standard deviation(σ) and particle concentration(N) for fine and coarse modes, and refractive index. The corresponding SSA is 0.85 for BC(wavelength independent) and 0.85 and 0.84 at 388 and 354 nm respectively for the OC model.

Table 2.

AOD	COD=5		COD=10	
	AOD	COD	AOD	COD
Z_{und} (2km)	40	4	26	9
Z_{ovr}(2km)	-19	-1	-12	-3
SSA_{und}(0.03)	-25	4	-23	1
SSA_{ovr}(0.03)	48	-5	43	-1
AAE_{und}(0.4)	23	3.	19	14
AAE_{ovr}(0.4)	-14	-1	-6	-5

Percent error in retrieved AOD and COD for an aerosol layer height uncertainty of 1km.

819 **Figure Captions**

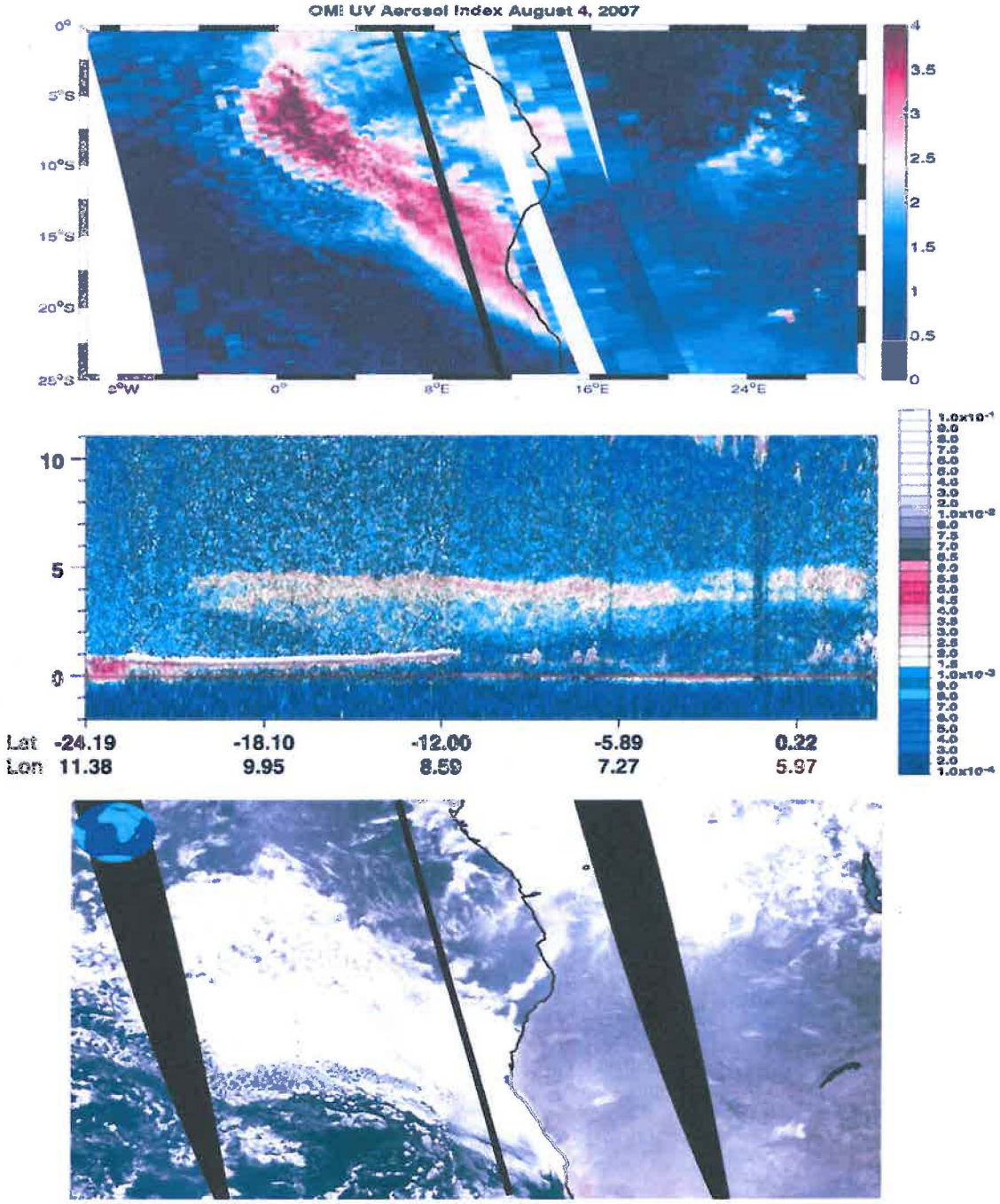

820
821 Figure1. OMI UV-AI (top panel), CALIOP back-scatter (middle panel), and MODIS true
822 color image composite (bottom panel) for an aerosol event observed on August 4, 2007
823 off the coast of Central Africa and over South East Atlantic Ocean. The CALIOP track
824 (thick black line) is also shown on UV-AI and RGB images.
825
826

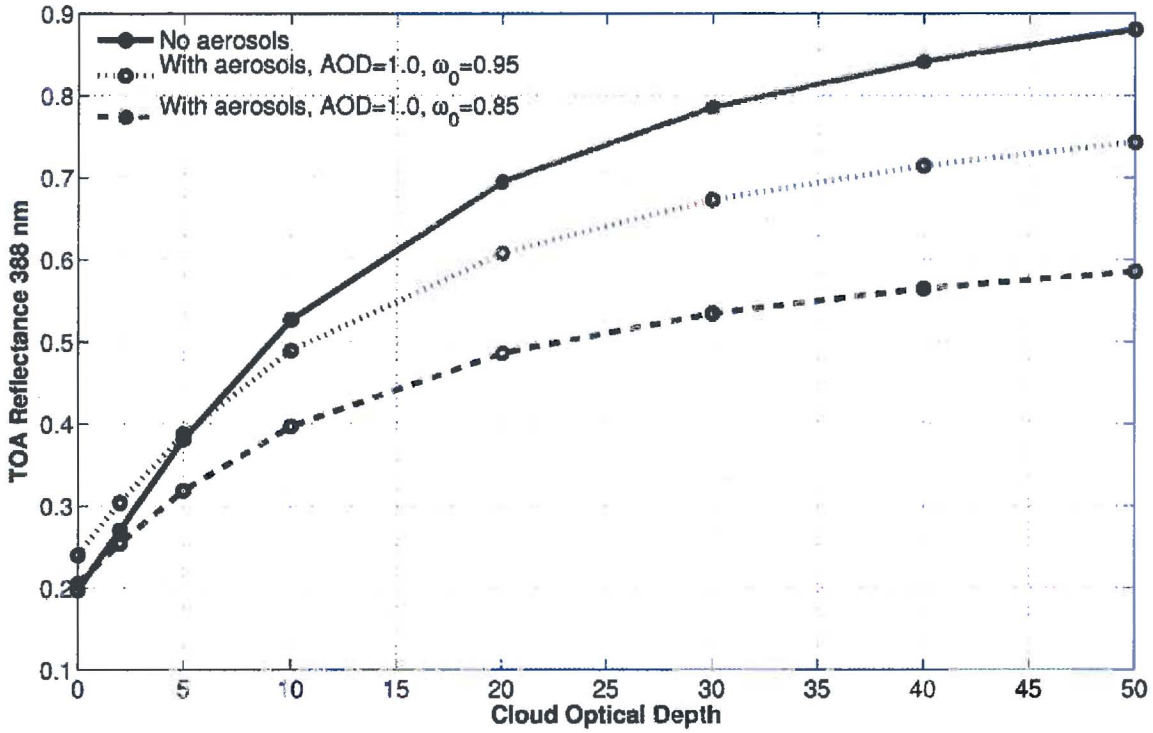

Figure 2. TOA reflectance sensitivity as a function of cloud optical depth for no-aerosol and for BC carbonaceous aerosol-laden atmosphere The cloud layer is located between 1.0 and 1.5 km and the aerosol layer is at 3km above the surface. Calculations were carried out for solar and satellite zenith angles 20° and 32° respectively, and relative azimuth angle 120°.

833

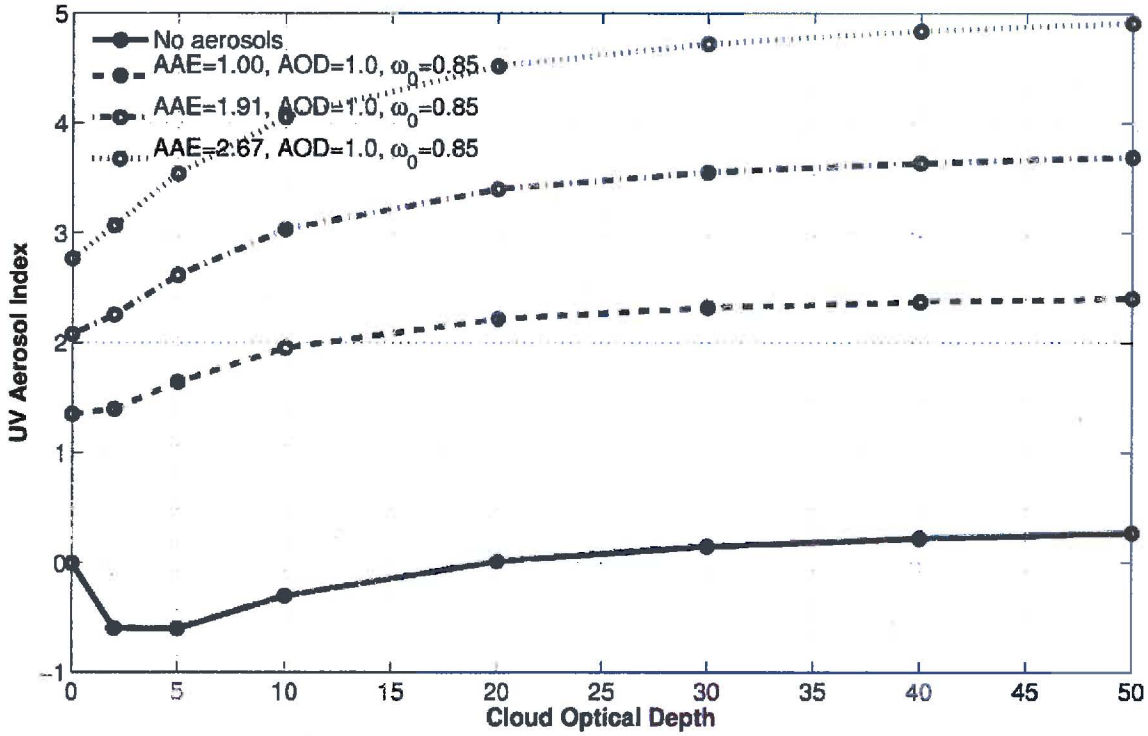

834

835 Figure 3. UV-aerosol index sensitivity to varying cloud optical depth for no aerosol, gray
836 aerosol and colored aerosol models. Aerosol and cloud location and viewing geometry as
837 in Figure 2.

838

838

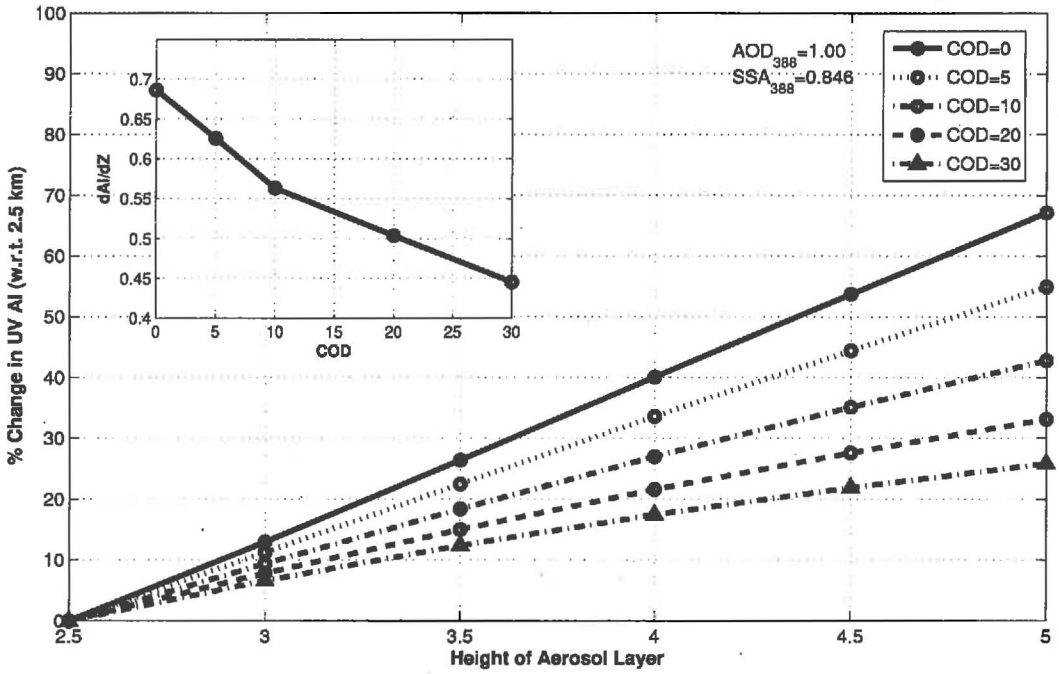

839
840

841 Figure 4. Relative change in UV-AI for varying aerosol mean height under different
842 values of cloud optical depth. Shown in inset is the derivative of AI w.r.t. height as a
843 function of cloud optical depth
844

844

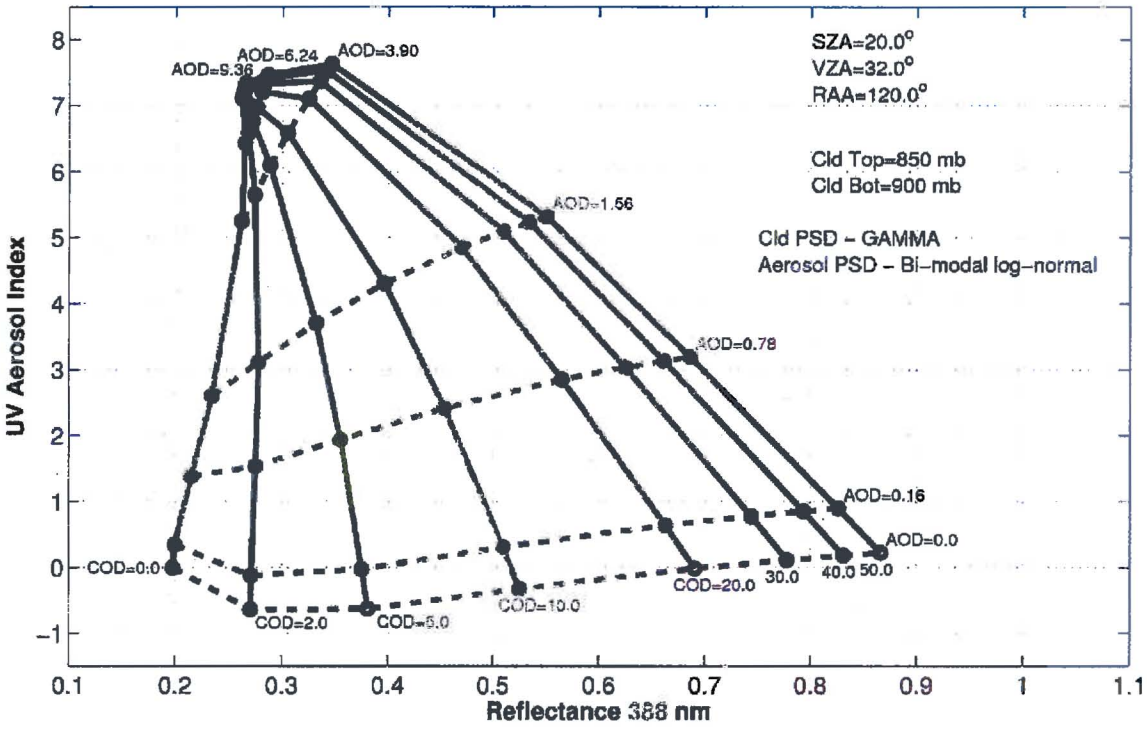

845

846 Figure 5. Retrieval domain of AAI Vs. Reflectance at 388 nm simulated using a radiative
847 transfer model for several values of AOD at 388 nm (0.0, 0.156, 0.780, 1.56, 3.9, 6.24,
848 9.36) and COD (0.0, 2., 5., 10., 20.,30,40,50).

849

849

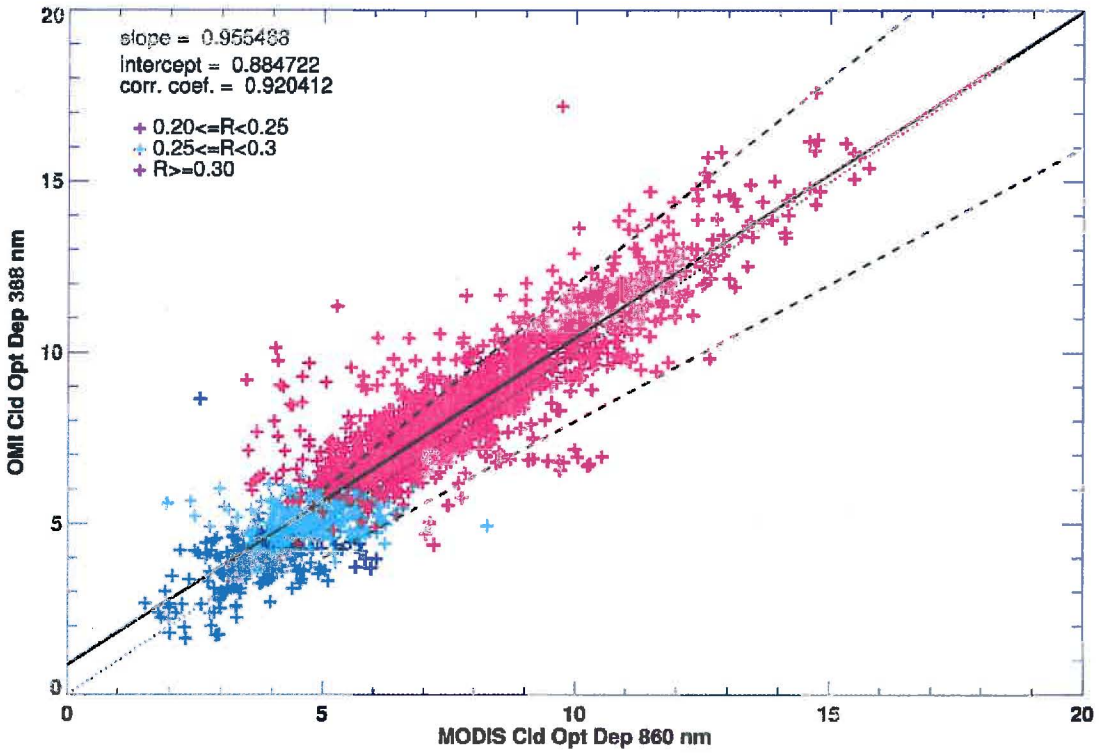

850

851 Figure 6. Comparison of MODIS and OMI cloud optical depth retrieved on October 13,
852 2006. No aerosols were present above clouds on this event. The dotted line indicates the
853 one-to-one agreement, the solid line is the linear fit, and the dashed lines represent the
854 ±20% uncertainty of the MODIS retrieval for COD's larger than 5. Significantly larger
855 uncertainty exists for COD smaller than 5 [*Platnick et al,* 2003].
856

856

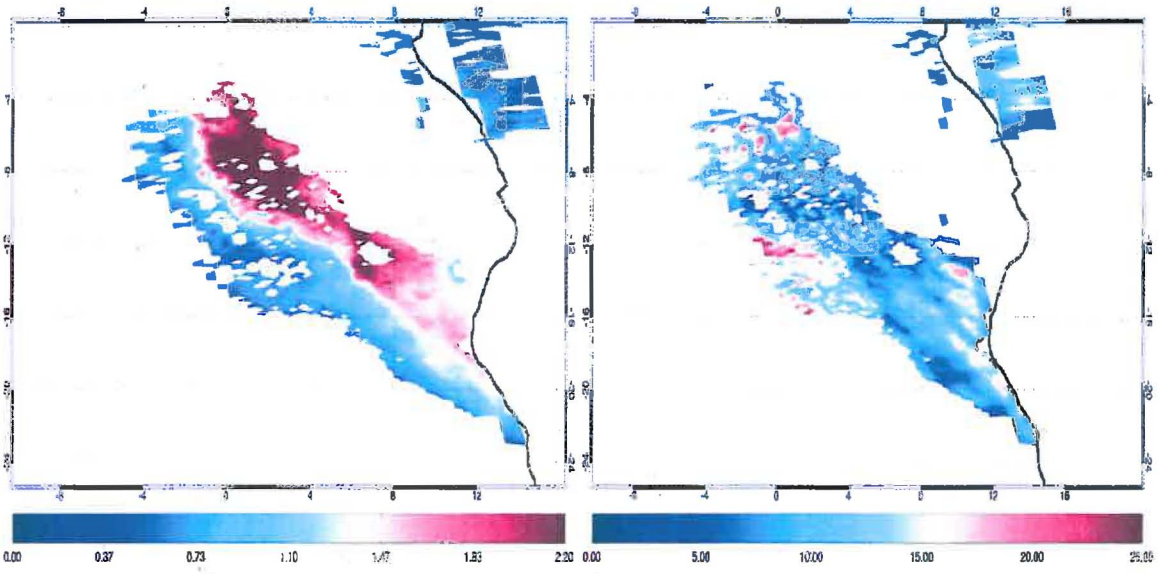

857
858 Figure 7. Spatial distribution of above-cloud AOD (388 nm) (left) and COD (right) for
859 the Aug 4, 2007 aerosol event.
860
861

861

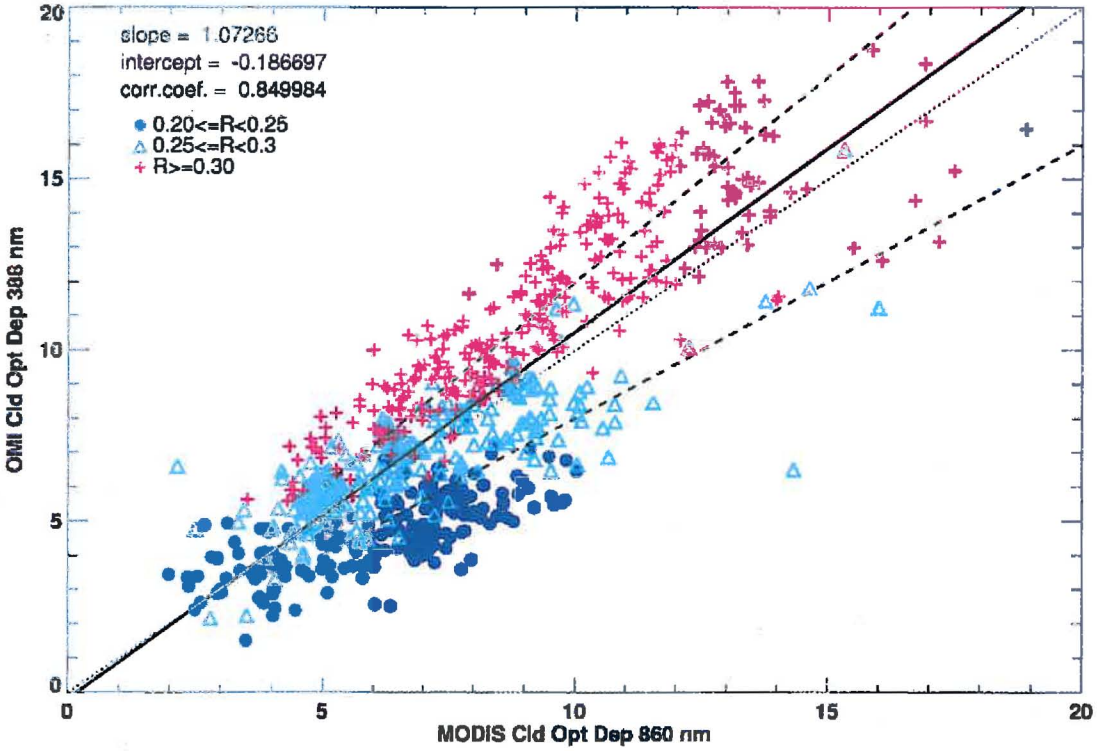

862
863 Figure 8. As in Figure 6 for the aerosol event over the Southeast Atlantic Ocean on Aug
864 4, 2007.
865

865

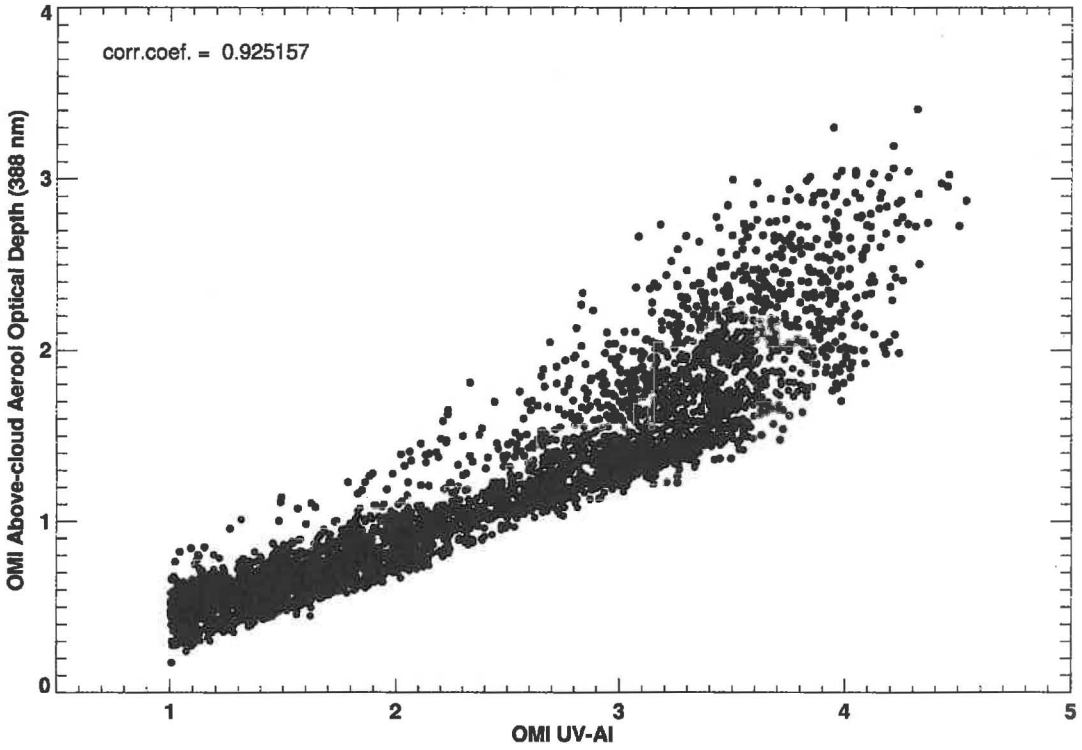

866
867 Figure 9. Relation between coincident aerosol optical depth and UV AI measured by
868 OMI on Aug 4, 2007 over the study region.
869

869

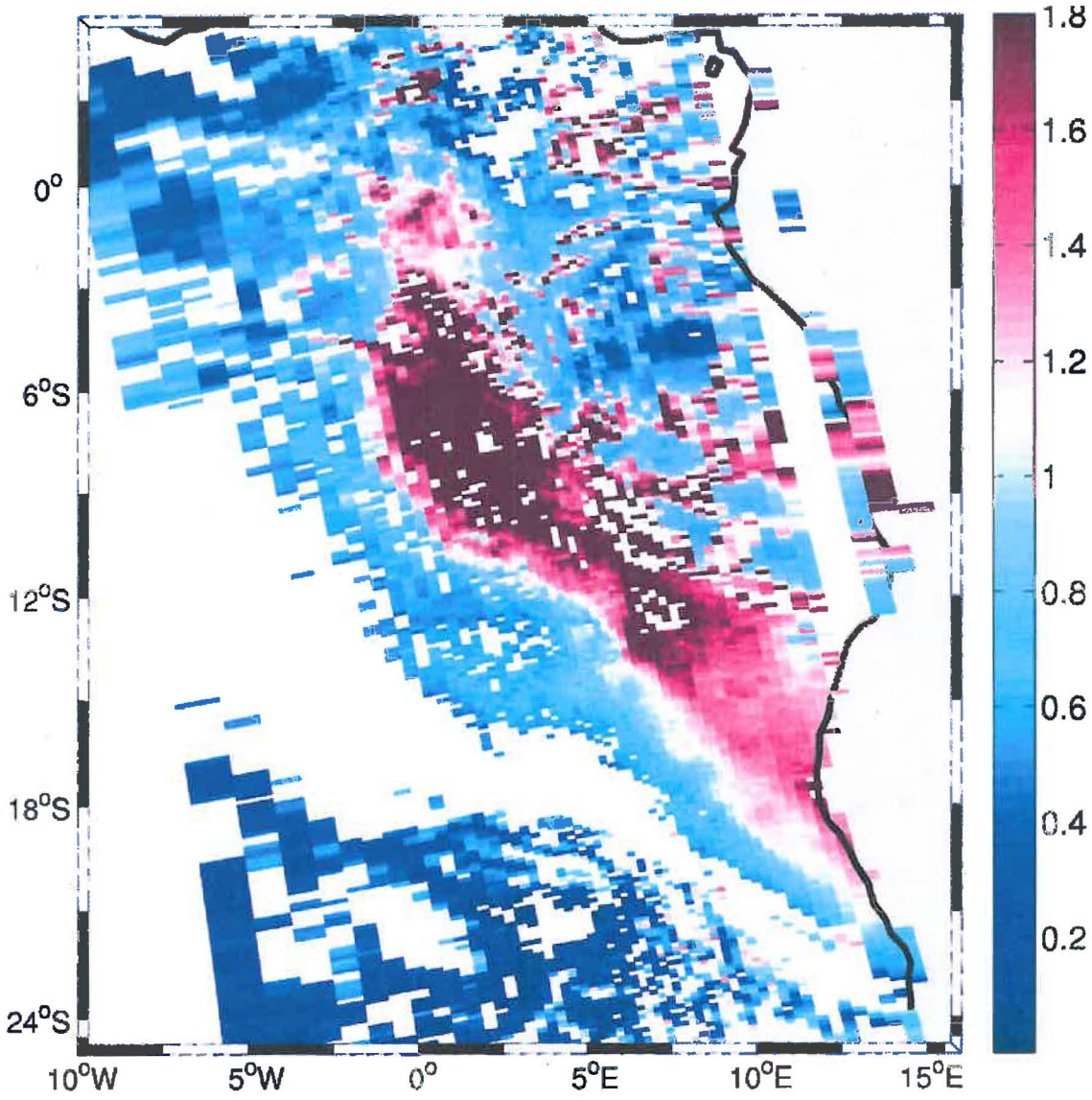

870
871 Figure 10. Composite of above-cloud and clear region AOD derived using cloud-aerosol
872 and only aerosol OMAERUV algorithm on Aug 4, 2007.
873

873

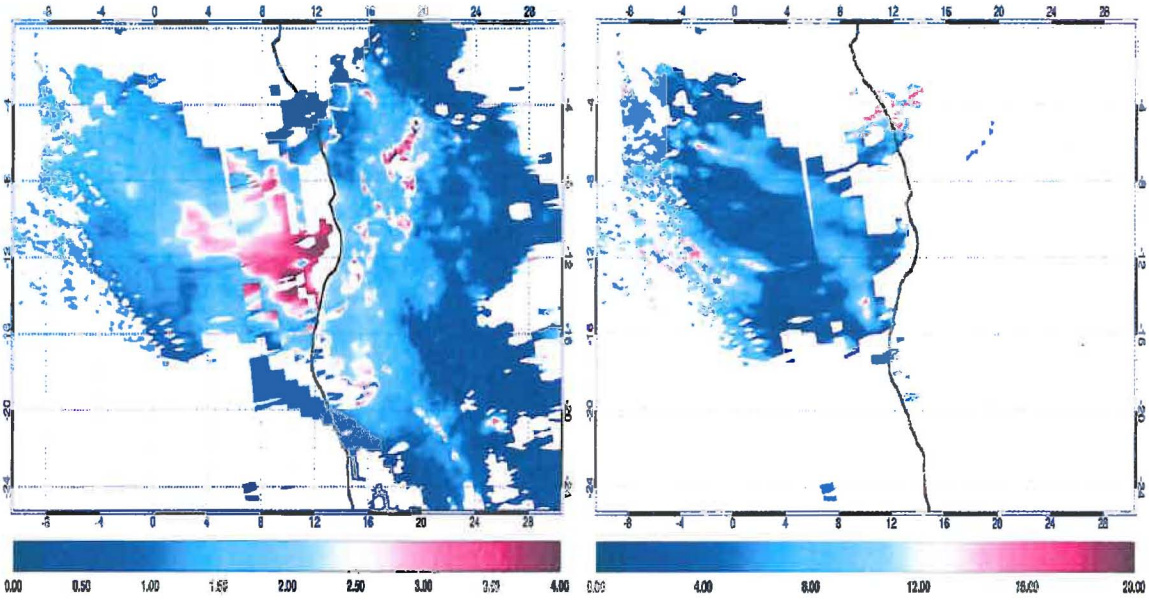

874
875
876 Figure 11. Retrieved AOD (left) and COD (right) fields on August 31, 2005.
877

877

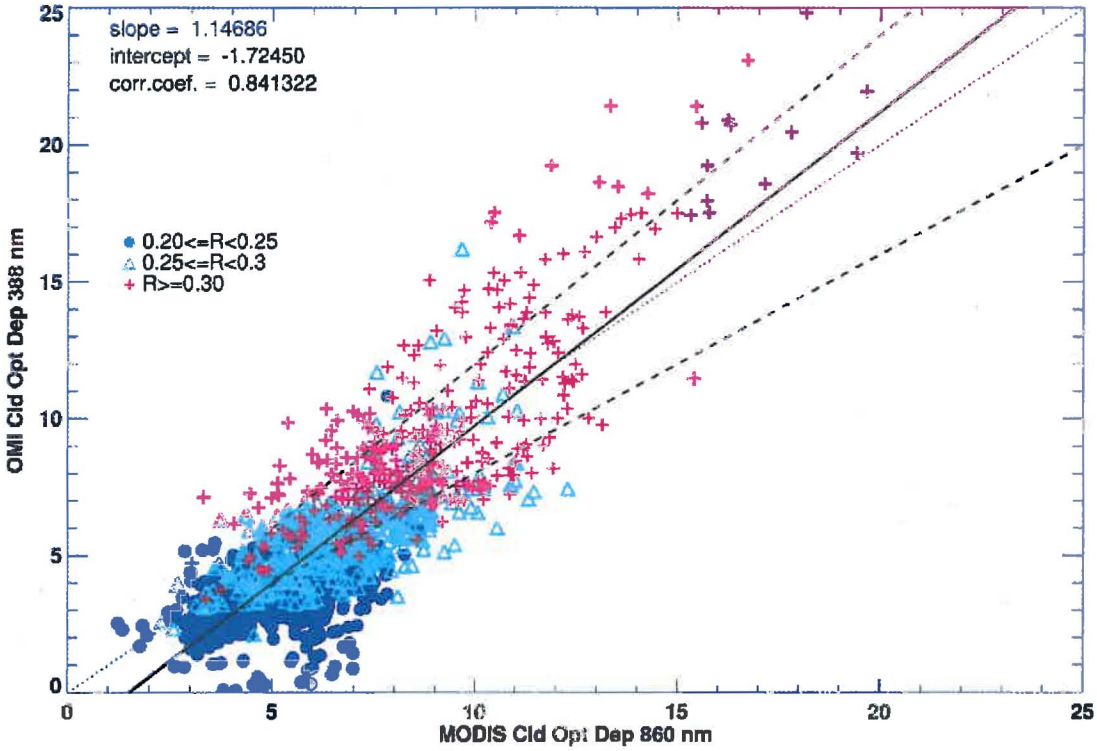

878
879 Figure 12. As in Figure 6 for the aerosol event over the Southeast Atlantic Ocean on
880 August 31, 2005
881

881

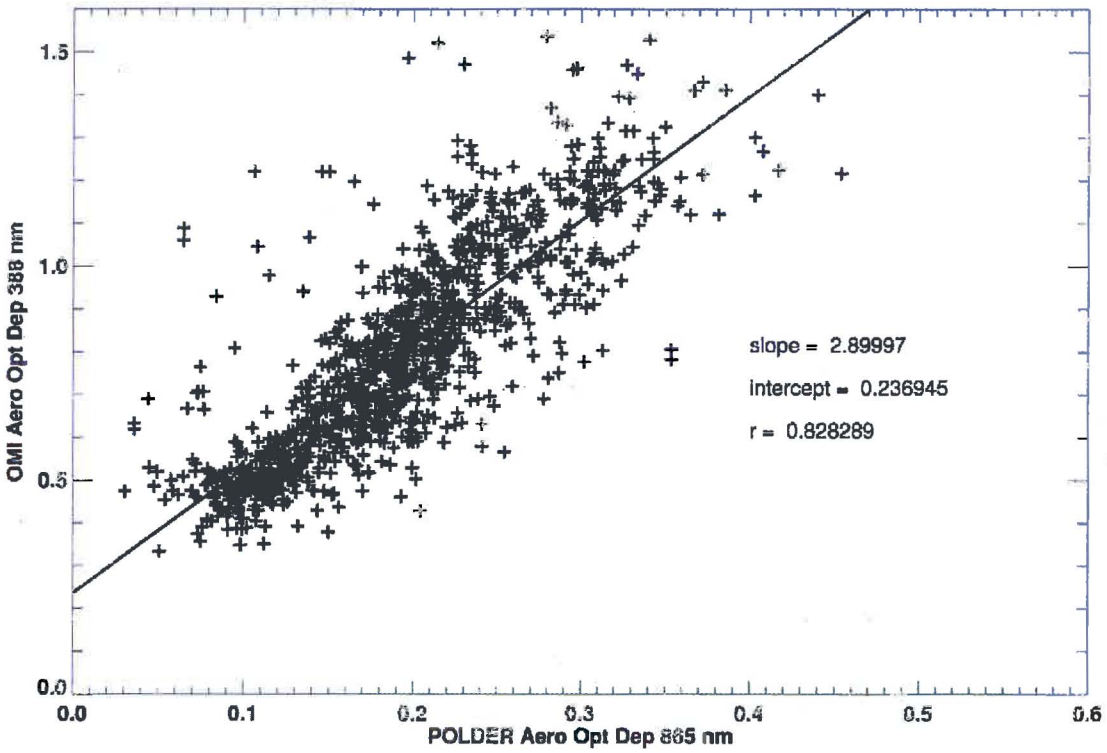

882
883 Figure 13. Scatter plot of retrieved 865 nm AOD from POLDER observation (x-axis)
884 and 388 nm AOD from OMI measurements on August 4, 2008. The difference in
885 magnitude is related to the small aerosols particle size and difference in reporting
886 wavelengths (see text for details).
887
888